Biomedical Microdevices 5:3, 245–251, 2003

BioMEMs and BioMedical Nanotechnology:

Section Editor Dr Mauro Ferrari

*Modeling of Microfabricated Microneedles for Minimally Invasive Drug Delivery, Sampling and Analysis**

D. Trebotich,[1]† *J.D. Zahn,*[2] *B. Prabhakarpandian,*[3] *and D. Liepmann*[1,2]

[1]*University of California, Berkeley, Department of Mechanical Engineering, Berkeley, CA 94720, USA*

[2]*University of California, Berkeley, Department of Bioengineering, Berkeley, CA 94720, USA*

[3]*CFD Research Corporation, Huntsville, AL 35805, USA*

Abstract. **We compare simulation to analysis and experiments for flows in three microneedle geometries—straight, bent and filtered. The bent microneedle was found to have the highest fluid carrying capacity of 0.082 ml/sec at 138 kPa with a Reynolds number of 738. A microneedle with a built in microfilter had a flow rate of 0.07 ml/sec. Although the throughput of these microneedles is low they compare favorably with other microneedle designs. Laminar flow models were found to accurately predict the flow behavior through the microneedles. All computational modeling was performed with the CFDRC CFD-ACE + suite of software tools.**

Key Words. **microneedles, microfluidics, computational model**

Introduction

Microneedle technology promises to revolutionize health care by allowing the precise injection of therapeutic agents to prescribed locations below the skin. In addition, microneedles can be used for sample collection for biological analysis, delivery of cell or cellular extract based vaccines, and sample handling providing interconnection between the microscopic and macroscopic world. Microneedles are desired because the small size and extremely sharp submicron tip radii reduce both insertion pain and tissue damage in the patient. Microneedles may be used for low flow rate continuous drug delivery such as the continuous delivery of insulin to a diabetic patient. Utilizing current micro electro mechanical systems (MEMS) technologies, different microneedle designs have been fabricated and integrated with various microfabricated microfluidic devices.

Previously, fluid flow in microneedles was studied experimentally (Zahn et al., 2000). Here, we first analyze flow in simple rectangular ducts in which exact solutions are known. We then use computational modeling capabilities to improve the analytical results by accounting for more complicated geometries in the actual designs. This will help us to further understand the experimental results and to optimize the design of medical microneedles and, thus, to shorten the whole design/fabrication cycle.

Analysis

For fully-developed, laminar flow the x-directed velocity profile in a rectangular duct with y and z cross section is given by Brody et al. (1996) and White (1991)

$$\begin{aligned} v_x = {} & \frac{16a^2}{\mu\pi^3}\left(-\frac{dP}{dx}\right)\sum_{i=1,3,5\ldots}^{\infty}(-1)^{(i-1)/2} \\ & \times\left[1-\frac{\cosh(i\pi z/2a)}{\cosh(i\pi b/2a)}\right]\frac{\cos(i\pi y/2a)}{i^3}, \\ & -a \le y \le a, \\ & -b \le z \le b, \end{aligned} \tag{1}$$

where $2a$ is the length of one of the walls, and $2b$ is the length of the other wall. Integrating this profile across y and z gives the average flow rate, Q as

$$Q = \frac{4ba^3}{3\mu}\left(-\frac{dP}{dx}\right)\left[1-\frac{192a}{\pi^5 b}\sum_{i=1,3,5\ldots}^{\infty}\frac{\tanh(i\pi b/2a)}{i^5}\right]. \tag{2}$$

*This work was originally presented as a plenary lecture: ''Complex Fluid Dynamics in BioMEMS Devices: Modeling of Microfabricated Microneedles'', *The Fifth International Conference on Modeling and Simulation of Microsystems*, pp. 10–13, Puerto Rico, USA, April 22–25, 2002.

†Lawrence Livermore National Laboratory, Livermore, CA 94551.

The average velocity, U, is $Q/(4ab)$. The pressure drop in the entrance region is estimated using the Blasius boundary layer solution over a flat plate (Leah, 1992; Denn, 1980; Blevins, 1992)

$$\tau_s = \frac{0.332\,\mu U}{x}\sqrt{\mathrm{Re}_x}, \tag{3}$$

where x is the distance along the plate, τ_s is the plate shear stress, μ is the dynamic viscosity and Re_x is the Reynolds number based on the distance x. If it is assumed that a rectangular duct behaves as a collection of four plates then the pressure gradient can be estimated as

$$\frac{dP}{dx} = -\frac{4\tau_s}{D_h}, \tag{4}$$

and the entrance pressure drop is found by integrating

$$\Delta P_{\mathrm{ent}} = \int_0^l \frac{4}{D_h}\tau_s\, dx = \frac{4(0.332)}{D_h} \sqrt{\rho\mu U^3}\int_0^l x^{-1/2}dx = \frac{8(0.332)}{D_h}\sqrt{\rho\mu U^3 l}, \tag{5}$$

where l is the entrance length or the needle length, whichever is shorter.

The entrance length is defined as the point where the pressure gradient was matched to that of the fully developed flow

$$\frac{dP}{dx} = -\frac{4\tau_s}{D_h} = \frac{-Q}{\frac{4ba^3}{3\mu}\left[1-\frac{192a}{\pi^5 b}\sum_{i=1,3,5\ldots}^{\infty}\frac{\tanh(i\pi b/2a)}{i^5}\right]}. \tag{6}$$

It should be noted that this entrance length estimate is about 20% of the standard macroscopic empirical entrance length estimate of Denn (1980)

$$\frac{l}{D_h} = 0.59 + 0.055\,\mathrm{Re}. \tag{7}$$

The entrance pressure drop is derived by make the simplifying assumption that the developing flow profile is a Blasius boundary layer and each wall in the flow channel is independent of each other, whereas the above equation is an empirical fit of measured data. Clearly the assumption made to derive the entrance pressure drop is not correct since each of the walls influence the fluid flow profile.

	Bent needle	Straight needle	Filter needle (before/after exp.)
Length (μm)	5,500	5,000	5,000/1,000
Width (μm)	160	80	80/1,350
Height (μm)	80	80	60/60
Hydraulic diameter (μm)	107	80	60/68.6

Fig. 1. *Needle parameters.*

Next, the losses due to viscous drag on the walls of the needle and geometric effects are modeled by applying the Modified Bernoulli equation. The pressure drop across the needle is Denn (1980)

$$\Delta P = \Delta P_{\mathrm{ent}} + \frac{1}{2}\rho\left(U_2^2 - U_1^2\right) + f\frac{L}{D_h}\frac{1}{2}\rho U^2 + K_{\mathrm{geom}}\frac{1}{2}\rho U^2, \tag{8}$$

where L is the needle length minus the entrance length. The fraction factor, f, is

$$f = \frac{4|\Delta P_{\mathrm{dev}}|}{\rho U^2}\frac{D_h}{L}, \tag{9}$$

where ΔP_{dev} is the fully developed pressure drop. K_{geom} is the geometric loss factor, which for a bent needle is Denn (1980)

$$K_{\mathrm{geom}} = 1.3, \tag{10}$$

while for a sudden contraction Denn (1980)

$$K_{\mathrm{geom}} = \left(\frac{2}{m} - \frac{A_2}{A_1} - 1\right)^2 \tag{11}$$

where m is the root of the quadratic

Needle type	Number of tests	Avg. exp. flow rate (ml/s)	Anal. flow rate (ml/s)	Error (%)	Reynolds number
Bent	4	0.082 ± 0.004	0.088	7.3	738
Reinforced	9	0.040 ± 0.004	0.040	0.0	503
Filter	2	0.070 ± 0.01	0.083	17.9	688
Double Channel	1	0.032	0.034	6.2	260

Fig. 2. *Experimental versus analytical flow rates at a constant pressure head of 138 kPa.*

$$\frac{1 - m(A_2/A_1)}{1 - (A_2/A_1)^2} = \left(\frac{m}{1.2}\right)^2 \tag{12}$$

and where A_1 and A_2 are the cross sectional areas before and after the contraction respectively.

Results and Discussion

We have predicted pressure drop versus volumetric flow rate (flow resistance) for steady, incompressible viscous flow through the three microneedle geometries and compare to analytical and experimental results (see Figure 1 and Figure 2 for needle parameters). All computations were performed using the CFD Research Corporation CFD-ACE + suite of tools. The numerical grids were created by the GEOM module of CFD-ACE + and are shown in Figure 3. The steady flow equations for a viscous, incompressible fluid were solved using the ACE(U) solver. The solver is based on a finite volume, pressure-based, strongly conservative formulation. It uses upwinding in its difference schemes when calculating derivatives and conjugate gradient methods when solving Poisson's equation. All data were post-processed in CFD-VIEW.

For a given flow rate, as determined by inlet conditions, the fluid pressure can be computed (Figure 4). As seen in Figure 5, the computed pressure drops compare well to both the experimentally measured and analytically modeled pressure drops in the needles. Discrepancies between simulations and measurements may be attributed to losses due to the experimental equipment not modeled in the simulations, or processing variances which lead to slightly different flow channel dimensions than were simulated. However, all simulation and analytical results fall within the experimental error bars.

One point of interest is to understand the velocity profile in the entrance region. When fluid enters a

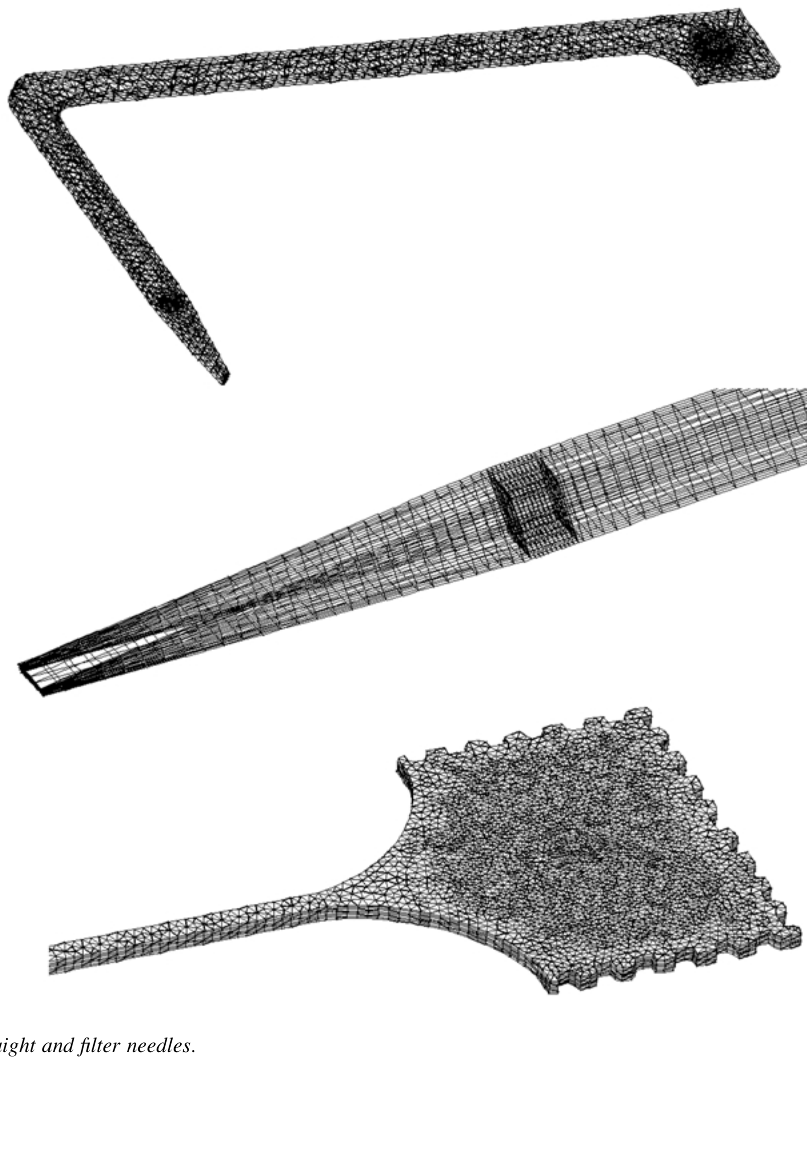

Fig. 3. *Grids for bent, straight and filter needles.*

Fig. 4. *Representative pressure distribution from CFD simulation in bent needle. The flow rate was set to 150 μl/min.*

channel, it enters with a flat velocity profile (plug flow) and eventually evolves into the classic parabolic flow profile. This transitional area is of importance since there is significant fluid drag on the sidewalls in the entrance region. The developing boundary layer has a sharper velocity gradient. Therefore, large molecules like proteins and DNA in a biological solution will see a strong extensional flow with a high wall shear upon entering a microneedle. The large forces on the molecules may be enough to induce cell lysis or shear induced chain excision of the proteins or DNA. Understanding of the development of the flow profile could lead to improved designs to limit wall shear stress to reduce shear-induced damage to biological molecules. As previously noted in the analysis, the entrance region was modeled as a collection of four independent plates over which a boundary layer was forming. This

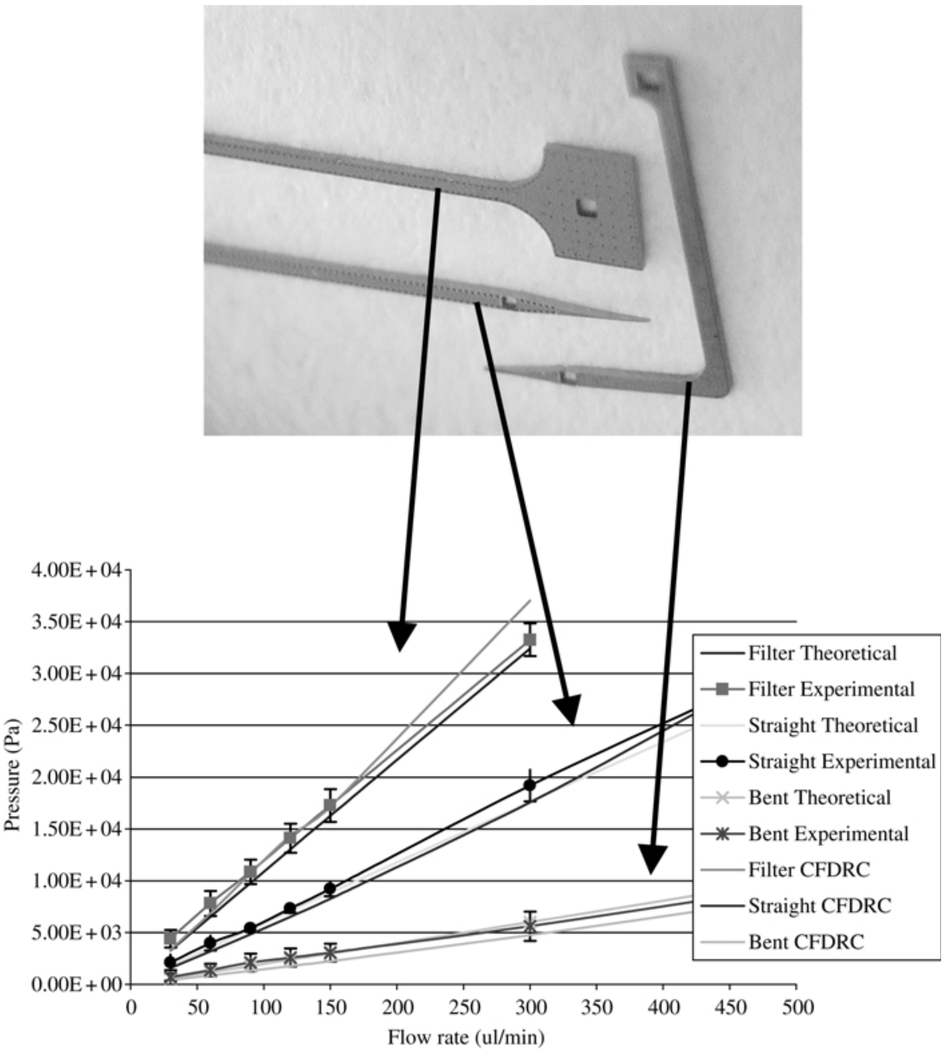

Fig. 5. *(Top) Needle geometries. (Bottom) Experimental, analytical and simulated flow resistances in different needle geometries.*

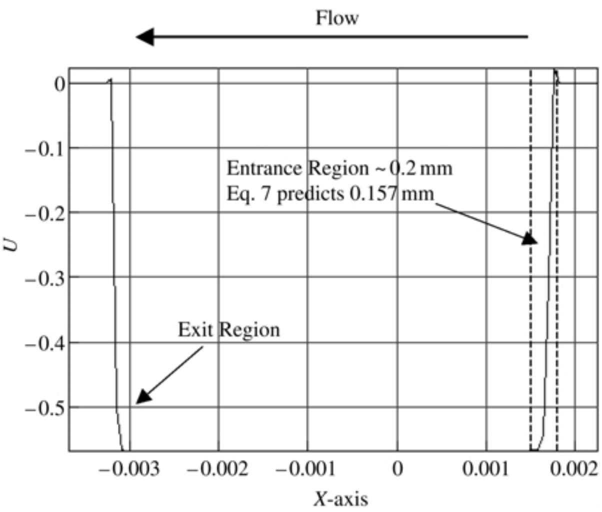

Fig. 6. *Centerline velocity profile in a straight needle at a flow rate of 120 μl/min.*

assumption is obviously incomplete, since the plates are not independent and the developing velocity profile is influenced by the four walls of the channel. In addition, the analysis used to obtain the pressure gradient (equation (6)) assumes a constant free stream velocity which enters the channel tangent to the flow direction. In reality, since the needle inlet is perpendicular to the flow channel direction (needle lumen), fluid enters orthogonal to the flow channel; the free stream velocity in the direction of the flow channel is thus zero at the entrance (Figure 6). And therefore, there is a gradient in the centerline velocity (extensional flow) not accounted for by the theory, which assumes a constant free stream velocity.

Figure 7 shows the x-component of the centerline velocity in a straight needle as predicted by the CFD model. The cross sectional velocity near the entrance region is a much flatter profile than the fully developed flow profile. By looking at the centerline velocity the entrance length may be estimated. Since the fluid is entering normal to the flow passage the x-component of velocity is initially zero. The flow proceeds from right to left. The entrance length can be estimated as the distance down the needle lumen to reach the maximum centerline velocity. From observation, the entrance length in the simulations corresponds more closely to the standard empirically derived macroscopic entrance length (equation (7)). This is not surprising since the analysis used to derive the analytical pressure gradient in the entrance region (equation (5)) makes several simplifying assumptions. This region is also not responsible for a significant pressure loss when compared to the viscous losses in the fully developed flow through the rest of the needle.

The wall strain rate may also be computed as a function of distance down the needle (see Figure 8). For a Newtonian fluid the wall shear stress is the strain rate times the fluid viscosity. The wall shear stress down the

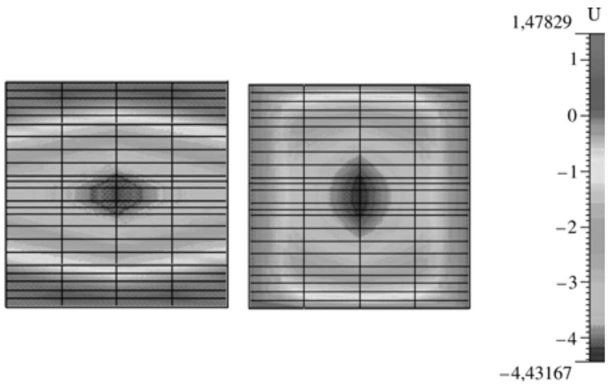

Fig. 7. *(Left) The x-directed velocity profile at the needle entrance. (Right) Fully developed x-directed velocity profile. (80 μm × 80 μm.)*

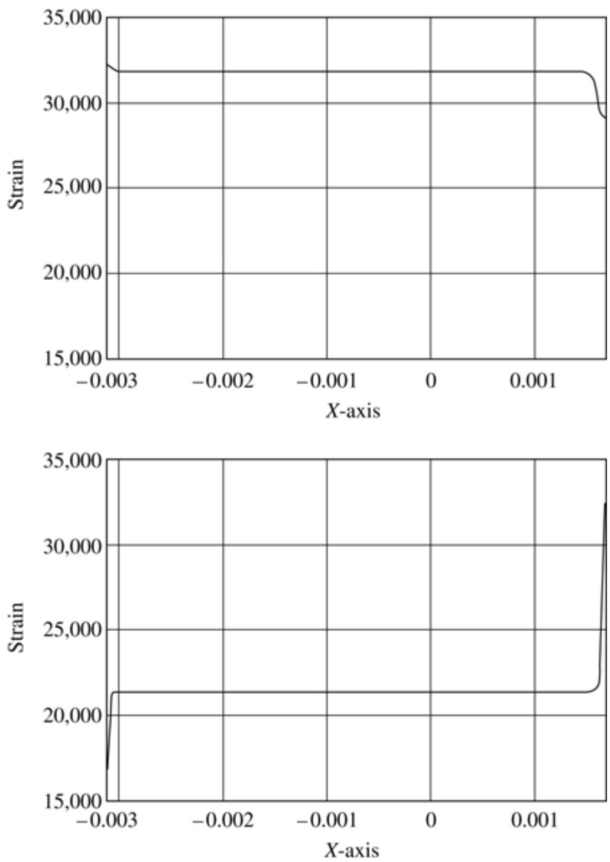

Fig. 8. *(Top) Strain rate along the wall of the microneedle down the centerline. Fluid entrance is at right and flow is to the left. (Bottom) Strain rate in the corner of the microneedle down the length of the needle. The fully developed strain rate is lower than the centerline. The flow rate is 120 μl/min.*

centerline of the needle in the entrance region is lower than the fully developed shear stress because the x-directed flow rate is initially zero. Therefore, the strain rate is initially lower, and gradually rises as the free stream velocity rises. However, in the corner of the needle the strain rate is much larger in the entrance region and thus drops off sharply; the fluid undergoes expansion to fill the whole channel volume upon entering the needle. It is important to see that for a Newtonian fluid the wall shear stress is over 300 Pa along the centerline and over 200 Pa in the corner of the needle, which could lead to damage of cells or biological molecules in a solution. The strain rates would also be greater at higher flow rates.

Computational modeling also makes it possible to visualize the velocity field near complicated structures such as a bend, filter posts or sudden expansion (Figure 9). We note that the largest error between theory and experiment occurred in the filter needles. This error is caused by the small spacing between the filter rungs. It can be shown that there is no boundary layer separation or recirculation around the bent needle. This is not surprising since the Reynolds number is less than 100 for all flows tested to obtain the experimental data for Figures 1 and 5. However, the detailed flow structure near the expansion in the filter needle shows some interesting features. First, there is a viscous recirculation of fluid around the filter rungs. This validates the analytical assumption that the filter must be thought of as a combination of channels in series as well as in parallel. Also, the majority of the velocity field stays in the center of the flow channel and proceeds directly to the outlet after the expansion. The outlet acts as a sink which pulls the streamlines towards it. In conclusion, the filter is less important to the pressure drop than the lumen of the needle. However, a filter could be more effectively placed as a series of posts in a line to the outlet through which the majority of fluid flows, rather than evenly distributed throughout the needle head.

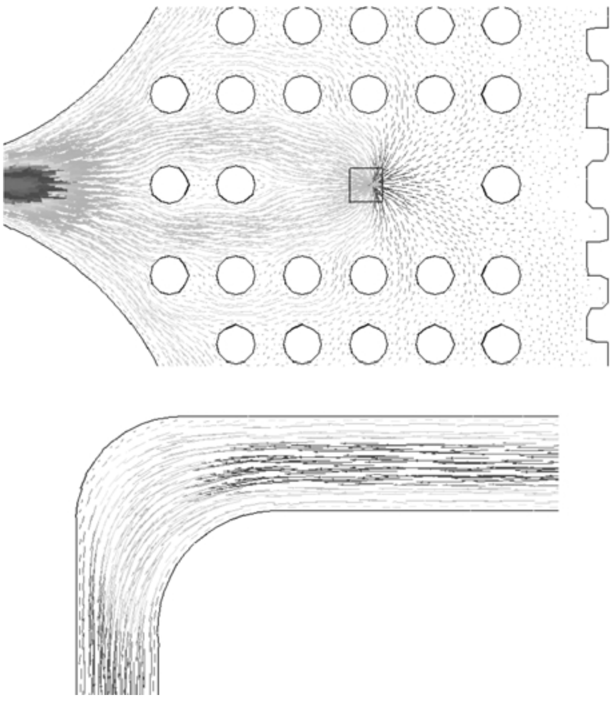

Fig. 9. (Top) Flow after a sudden expansion in the filter microneedle. (Bottom) Flow around a bend in a microneedle.

Conclusions

The computational models presented here agree well with experimental and analytical models. The simulation and analytical results are contained within the experimental error bars. There are no real surprises for these flows which are viscous dominated and essentially 2-dimensional in the duct. However, analytical models break down in complex geometries and at the entrance. CFD enables us to look at the velocity, pressure and strain distributions in these cases. This information feeds back into the design cycle for drug delivery as it allows us to balance drug delivery rates with needle strength/ mechanical behavior for making better needles.

As future work we will consider the physics of biological fluids that actually flow in microneedles. Initially, the current models can be extended to address simple non-Newtonian fluids, namely shear-thinning or inelastic fluids. More complicated non-Newtonian fluid models which better represent polymers that exist in biological solutions (viscoelasticity) would have to be addressed with more elaborate models (Trebotich et al., 2003). The effects of these more appropriate fluid models should be seen in shearing regions, especially in areas of extensional flow which are of interest in the devices modeled here.

Acknowledgment

This study was supported by the Defense Advanced Research Projects Agency's (DARPA) μFLUMES program.

References

R.D. Blevins, *Applied Fluid Dynamics Handbook*, (Krieger Publishing Company, Malabar, Florida, 1992).

J.P. Brody, P. Yager, R.E. Goldstein, and R.H. Austin, Biophysical Journal **71**, 3430–3441 (1996).

M.M. Denn, *Process Fluid Mechanics*, Prentice Hall International Series in the Physical and Chemical Engineering Sciences, 1980.

L.G. Leah, *Laminar Flow and Convective Transport Processes. Scaling Principles and Asymptotic Analysis* (Butterworth-Heinemann Series in Chemical Engineering, Boston, MA, 1992).

D. Trebotich, P. Colella, G. Miller, and D. Liepmann, *Technical Proceedings of the 2003 Nanotechnology Conference and Trade Show, NanoTech 2003*. San Francisco, CA, Feb. 23–27, 520–523 (2003).

F.M. White, *Viscous Fluid Flow*, 2nd edn (McGraw-Hill Book Company, New York, NY, 1991).

J.D. Zahn and D. Liepmann, Proceedings of the ASME IMECE MEMS 2000 Symposium, 647–653 (2000).

J.D. Zahn, N.H. Talbot, D. Liepmann, and A.P. Pisano, Biomedical Microdevices **2**(1), 295–303 (2000).